Tucci, C.; Trujillo Guillen, M.; Berjano, E.; Iasiello, M.; Andreozzi, A.; Vanoli, GP. (2022). Mathematical modeling of microwave liver ablation with a variable-porosity medium approach. Computer Methods and Programs in Biomedicine. 214:1-9. https://doi.org/10.1016/j.cmpb.2021.106569

Mathematical modeling of microwave liver ablation with a variable-porosity medium approach

Claudio Tucci[1], Macarena Trujillo[2], Enrique Berjano[3], Marcello Iasiello[4], Assunta Andreozzi[4], Giuseppe Peter Vanoli[1]

[1] Dipartimento di Medicina e Scienze della Salute "Vincenzo Tiberio", Università del Molise, Via Francesco De Sanctis 1, 86100, Campobasso, Italy

[2] BioMIT, Department of Applied Mathematics, Universitat Politècnica de València, Camino de Vera, 46022, Valencia, Spain

[3] BioMIT, Department of Electronic Engineering, Universitat Politècnica de València, Camino de Vera, 46022, Valencia, Spain

[4] Dipartimento di Ingegneria Industriale, Università degli Studi di Napoli Federico II, P.le Tecchio 80, 80125, Napoli, Italy

Corresponding author: c.tucci1@studenti.unimol.it

Abstract

Background and objectives: Thermal ablation of tumors plays a key role to fight cancer, since it is a minimally invasive treatment which involves some advantages compared to surgery and chemotherapy, such as shorter hospital stays and consequently lower costs, along with minor side effects. In this context, computational modeling of heat transfer during thermal ablation is relevant to accurately predict the obtained ablation zone in order to avoid tumor recurrence risk caused by incomplete ablation, and the same time to save the surrounding healthy tissue. The aim of this work is to develop a more realistic porous media-based mathematical model to simulate a microwave thermal ablation (MWA) of an in vivo liver tumor surrounded by healthy tissue.

Methods: The domain is made up of a spherical tumor bounded by a cylindrical healthy liver tissue. The simulated microwave antenna is a 14 G HS Amica-Gen Probe, and the supplied power of 60 W is applied for 300 s and 600 s. The model consists in coupling modified Local Thermal Non Equilibrium (LTNE) equations with the electromagnetic equations. The LTNE equations include a variable porosity function which fits the porosity changing from the tumor core to the rim based on experimental measures in *in vivo* cases. Moreover, four different blood vessels' uniform distributions are investigated to compare the effects of different vascularizations of the considered target tissue.

Results: The results are shown in terms of temperature fields, ablation diameters and volumes based on the Arrhenius thermal damage model with 99% of cell death probability. The outcomes show a very good agreement with a clinical study on human patients with hepatocellular carcinoma using the same antenna and energy setting, when terminal arteries distribution is included.

Conclusions: In this work, an *in vivo* microwave ablation of liver tumor surrounded by healthy tissue is modeled with a variable-porosity medium approach based on experimental measures. The outcomes shown for distinct vascularizations underline the key relevance of modeling more and more accurately tumor MWA, by considering increasingly realistic features, avoiding tumor recurrence, and improving both medical protocols and devices.

Keywords: Bioheat equation; numerical modeling; microwave ablation, porous media model; variable porosity.

Nomenclature

a	Volumetric transfer area (m^{-1})	V	Volume (m^3)
a_1	Coefficient (m^{-2})	z	Spatial coordinate (m)
A	Frequency factor (s^{-1})	*Greek symbols*	
b_1	Coefficient (m^{-1})	β	Coefficient (-)
c	Specific heat (J kg^{-1} K^{-1})	ΔE	Activation energy (J mol^{-1})
c_1	Coefficient (-)	ε	Porosity (-)
C_w	Water content (%)	ε_0	Free space permittivity (F m^{-1})
d	Diameter of blood vessel (m)	ε_r	Relative permittivity (-)
d_c	Diameter of the ablation zone (m)	μ_r	Relative permeability ratio (-)
E	Electric field vector (V m^{-1})	ρ	Density (kg m^{-3})
h_c	Convective interfacial heat transfer coefficient (W m^{-2} K^{-1})	σ_e	Effective electric conductivity (S m^{-1})

h_{fg}	Product of water latent heat of vaporization and water density at 100°C (J m^{-3})	τ	Time integration variable (s)
h_r	Convective coefficient to model the electrode cooling system (W m^{-2} K^{-1})	ω	Angular frequency (rad s^{-1})
k	Thermal conductivity (W m^{-1} K^{-1})	Ω	Thermal damage (-)
k_0	Propagation constant in the free-space	*Subscripts*	
P	Cell death probability (%)	b	Blood
q_c	Convective heat flux (W m^{-2} K^{-1})	g	Referred to temperatures above 100°C
Q_{ext}	External power density (W m^{-3})	int	Intermediate
r	Spatial coordinate (m)	l	Referred to temperatures below 100°C
R	Universal gas constant (J mol^{-1} K^{-1})	max	Maximum
t	Time (s)	min	Minimum
T	Temperature (K)	nec	Necrosis
T_r	Coolant temperature (K)	t	Tissue
$\mathbf{u}$	Velocity vector (m s^{-1})	tum	Tumor
		var	Variable

1. Introduction

Thermal ablation of tumors plays a key role in fighting cancer, since it is a minimally invasive treatment which involves some advantages compared to surgery and chemotherapy, such as shorter hospital stays and consequently lower costs, along with minor side effects [1-3]. The treatment consists in focusing an energy source (generally radiofrequency or microwave) on the tumor by means of an applicator. When the tissue temperature exceeds 55-60 ºC for some seconds, complete necrosis occurs. However, lower temperatures can obtain the same goal with a longer exposure [4, 5]. The main critical issue about thermal ablation is the tumor recurrence risk caused by incomplete ablation (i.e. the ablation zone does not completely cover the tumor), which is higher when ablative temperatures are not achieved [6]. As concerns this criticality, tumor zones where ablative temperatures do not occur, namely the periablational areas, can be interested by tumor regrowth [7], so this area must be minimized [8]. In this context, computational modeling of heat transfer in thermal ablation is relevant to predict the obtained ablation zone accurately, in order to improve current medical devices and protocols. For this purpose, various bioheat models have been developed over the years, starting from Pennes' equation [9], which is the simplest bioheat model, still widely used, but characterized by several shortcomings such as the neglected blood flow direction and the artery-vein countercurrent arrangement. It also simplifies the real scenario by assuming the thermal equilibrium between venous blood and tissue, and constant arterial blood temperature of 37 °C during the ablation treatment. Over the years, many studies have been interested in developing more and more accurate bioheat models [10,11], and differences have been highlighted among the results obtained [12,13]. One of the most promising models is the porous media-based [14] local thermal non equilibrium (LTNE), formerly developed by Xuan and

Roetzel [15] and then modified several times throughout the years [16-22] to consider different tissue properties, vascular structures, and biomedical applications [23-26]. A common limit to all these models is that they neglect the variation in blood volume fraction (namely the porosity variation) inside the tumor, and between the tumor and the surrounding healthy tissue. The blood volume fraction, indeed, varies between the tumor domain and the healthy tissue, as experimentally measured in *in vivo* by Stewart et al [27].

On these basis, microwave (MW) ablation (MWA) of a spherical tumor surrounded by healthy liver tissue is simulated in this work. The thermal problem is modeled by means of LTNE equations modified to include the water content vaporization in the blood phase and tissue phase (both in healthy tissue and tumor) separately, as done in [13], and the porosity variation in the domain with a changing in space function from the core to rim of the tumor. In the adjacent healthy tissue, instead, a constant porosity value is considered. Both the microwave antenna and ablation protocol are simulated mimicking the same conditions of a clinical study on human patients [28], in order to compare computer and clinical results and achieve model validation. Four different types of blood vessels are considered to be in the liver tissue separately in order to assess the key relevance of the vascular structure in *in vivo* situations. The main goal of thermal ablation is the complete tumor ablation avoiding its recurrence, so the objective of this study is to develop a more realistic *in vivo* numerical bioheat model, able to predict the ablation zone size more accurately, and consequently improve medical protocols and devices.

2. Materials and Methods

2.1. Mathematical model

The geometry of the model is shown in Figure 1 and consists of a 5 cm radius and 10 cm height cylindric liver domain, which includes a spherical tumor of radius 1.2 cm, and the surrounding healthy tissue. As regards the MW antenna, a 20 cm long, 14 G applicator is modeled, with a mini-choke which simulates the HS Amica-Gen device (HS AMICA PROBE, HS Hospital Service, Aprilia, Italy) used in [28]. The symmetry of the problem allows to use a 2D axisymmetric model to reduce computing time.

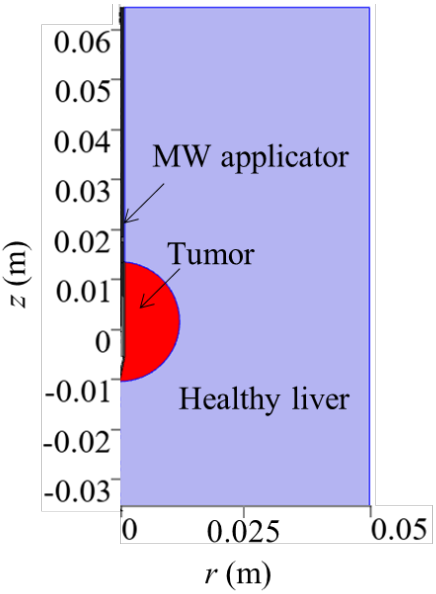

Figure 1. Two-dimensional axisymmetric model consisting of a spherical tumor bounded by healthy liver tissue and an internally cooled MW applicator.

As regards the employed equations, the thermal problem is coupled with the electromagnetic one. To solve the temperature field inside the tissue domain, a porous media-based model is conveniently modified to overcome the shortcomings of the simplest Pennes' bioheat equation [9], and to obtain more realistic results compared to the experimental results. According to the porous media theory [14], the biological tissue is modeled considering two distinct phases that coexist in the same domain: the solid phase

(tissue phase) that consists of tissue cells and the interstitial spaces among them, and the fluid phase (blood phase) which represents the blood flowing through the tissue. The first mentioned phase is the so called “extravascular region”, while the second one is named “vascular region”. In addition, blood and tissue phases are considered to be at different temperature, so the Local Thermal Non-Equilibrium assumption is employed, and two different energy equations can be written as follows similarly to Amiri and Vafai [29] by considering the variable-porosity assumption. For the tissue phase:

$$\left(1-\varepsilon_{var}\right)\left(\rho c\right)_t \frac{\partial \left\langle T_t \right\rangle}{\partial t} = \nabla \cdot \left(\left(1-\varepsilon_{var}\right) k_t \nabla \left\langle T_t \right\rangle\right) - h_c a \left(\left\langle T_t \right\rangle - \left\langle T_b \right\rangle\right) + \left(1-\varepsilon_{var}\right) Q_{ext} \tag{1}$$

and for the blood phase:

$$\varepsilon_{var} \left(\rho c\right)_b \left(\frac{\partial \left\langle T_b \right\rangle}{\partial t} + \beta \left\langle \mathbf{u} \right\rangle \cdot \nabla \left\langle T_b \right\rangle \right) = \nabla \cdot \left(\varepsilon_{var} k_b \nabla \left\langle T_b \right\rangle\right) + h_c a \left(\left\langle T_t \right\rangle - \left\langle T_b \right\rangle\right) + \varepsilon_{var} Q_{ext} \tag{2}$$

where ε_{var} is the variable porosity considered in the tissue (namely the blood volume fraction in the entire tissue volume), ρ is the density, c is the specific heat, T_t and T_b are the tissue and blood temperatures, respectively, k is the thermal conductivity, t is the time, $\mathbf{u}$ is the blood velocity vector, h_c is the interfacial heat transfer coefficient (considered constant and equal to 170 W m^{-2} K^{-1} as in [30]), and a is the volumetric transfer area between tissue and blood, which is evaluated from the hydraulic diameter definition in porous media as:

$$a = \frac{4\varepsilon_{var}}{d} \tag{3}$$

where d is the blood vessel diameter. Moreover, the coefficient β from Eq. (2) is assumed to be 0 or 1 depending on the value of the thermal damage function Ω, which is defined according to the Arrhenius model from an exponential relationship between tissue exposure

temperature, time and the kinetic parameters that account for morphologic changes in tissue relating to the thermal degradation of proteins [31] as:

$$\Omega(t) = \int_0^t A e^{-\frac{\Delta E}{RT_t(\tau)}} d\tau \tag{4}$$

where A is the frequency factor, ΔE the activation energy for the irreversible damage reaction and R is the universal gas constant. In our study, $A = 7.39 \times 10^{39}$ s^{-1} and $\Delta E = 2.577 \times 10^5$ J mol^{-1} for healthy liver tissue, while for the liver tumor $A = 3.247 \times 10^{43}$ s^{-1} and $\Delta E = 2.814 \times 10^5$ $Jmol^{-1}$ [32].The D99 thermal damage contour is employed as in [8] to evaluate the thermal damage contour, i.e. the isoline $\Omega = 4.6$ which corresponds to 99% of cell death probability according to the following equation:

$$P = 1 - e^{-\Omega(t)} \tag{5}$$

Thus, when the 99% cell death probability is reached, β becomes zero and consequently blood velocity is zero too, since there is no blood flow in coagulated tissue.

In addition, the volume averaging technique is employed to consider the volume average quantities of the variables [14], so that the symbol <> refers to the average volume of a generic variable and is neglected from this point onwards.

The blood volume vascular fraction is the key parameter of the porous media models, because it affects the temperature outcomes [13, 14, 33, 34]. So its importance grows as the porosity of the considered organ increases, such as in liver. The larger the porosity value, the larger the convective contribution of the mass blood flow, and the lower the obtained temperature because of the blood heat sink effect [13]. Different values of blood volume fractions have been measured for liver in distinct physiological conditions, such as healthy, cirrhotic liver, and in chronic liver hepatitis [35-38]. The focus here is on the spatial

porosity variability from the tumor core to the adjacent healthy tissue which should be included in MWA modeling in order to improve predictions. The hepatic blood volume value increases from the tumor core to the rim according to the experimental *in vivo* measures by Stewart et al. [27] in a rabbit liver tumor model. This study hence highlights that the minor microvascular function in tumor core leads to lower values of blood volume fraction, while the higher values measured in tumor rim suggest a high nutritive flows in that region. To consider this phenomenon, we assumed a quadratic function to describe this behavior, considering the minimum porosity value in the tumor core, the intermediate value in the tumor rim, and the maximum value in the adjacent healthy tissue as follows:

$$\varepsilon_{var} = \begin{cases} a_1(r^2 + z^2) + b_1 r + c_1 & \textit{tumor domain} \\ \varepsilon_{max} & \textit{healthy liver domain} \end{cases} \tag{6}$$

where the coefficients a_1, b_1 and c_1 are obtained imposing the following conditions:

$$\begin{cases} \varepsilon_{var}|_{r,z=0} = \varepsilon_{min} \\ \varepsilon_{var}|_{r,|z|=r_1} = \varepsilon_{int} \\ \dfrac{\partial \varepsilon_{var}}{\partial r_{r=0}, \partial z_{z=0}} = 0 \end{cases} \tag{7}$$

so using the values obtained in [27] for the blood volume fractions 16 days after the tumor implantation in rabbits. Thus, the obtained coefficients a_1, b_1 and c_1 are consequently obtained as follow:

$$a_1 = \frac{\varepsilon_{int} - \varepsilon_{min}}{r_1^2} \tag{8}$$

$$b_1 = 0 \tag{9}$$

$$c_1 = \varepsilon_{min} \tag{10}$$

where r_1 = 1.2 cm corresponds to the tumor rim. Figure 2 shows the porosity function in both r and z directions for the tumor domain, showing that the constant porosity curves rise quadratically from the core to the periphery of the tumor.

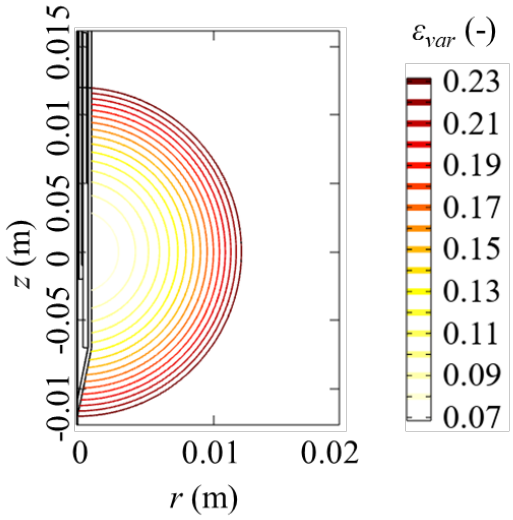

Figure 2. 2D plot for quadratic porosity function inside the tumor. Porosity increases from the tumor core to the rim according to the experimental in vivo measures by Stewart et al. [27] in a rabbit liver tumor model.

In this study, evaporation occurs because temperatures are higher than 100 °C. In order to include this effect, the LTNE model is modified as done in [13] for healthy tissue, including in addition the evaporation of the different water content also in tumor and blood separately. The enthalpy method is used as described by [39], so the term (ρc) in Eqs. (1) and (2) becomes:

$$(\rho c)_{b,t} = \begin{cases} (\rho_l c_l)_{b,t} & 0\ ^\circ\mathrm{C} < T_{b,t} \le 99\ ^\circ\mathrm{C} \\ \dfrac{h_{fg} C_w}{\Delta T_{b,t}} & 99\ ^\circ\mathrm{C} < T_{b,t} \le 100\ ^\circ\mathrm{C} \\ \rho_g c_g & T_{b,t} > 100\ ^\circ\mathrm{C} \end{cases} \tag{11}$$

where ρ_l and c_l are density and specific heat at temperatures below 100°C (liquid phase), ρ_g and c_g are density and specific heat at temperatures above 100°C (gas phase), h_{fg} is the product of water latent heat of vaporization and water density at 100°C, and C_w is the water content inside the healthy tissue (68%), the tumor liver tissue (81%) or blood (79%), respectively, as reported in literature [40, 41]. The temperature difference $\Delta T_{b,t}$ is assumed to be equal to 1°C [39].

The heat source Q_{ext} is obtained from the distribution of the electrical field vector **E** of the electromagnetic problem as:

$$Q_{ext} = \frac{1}{2}\sigma_e |\mathbf{E}|^2 \tag{12}$$

where σ_e is the effective conductivity at 2.45 GHz and |**E**| is the Euclidian norm of **E**. The electric field distribution is obtained from the Helmholtz equation as follows:

$$\nabla \times \mu_r^{-1}(\nabla \times \mathbf{E}) - k_0^2 \left(\varepsilon_r - \frac{j\sigma_e}{\omega \varepsilon_0} \right) \mathbf{E} = 0 \tag{13}$$

where μ_r is the relative permeability ratio, which is 1 for all the materials considered, k_0 is the propagation constant in the free-space, ε_r is the relative permittivity, ε_0 is the permittivity of the free space and ω is the angular frequency.

Both the effective electric conductivity σ_e and the relative permittivity ε_r, are considered temperature dependent as in [8, 42], so are defined as follows:

$$\sigma_e(T) = \sigma_e(37^\circ\mathrm{C}) \cdot \left(1 - \frac{1}{1 + \exp(6.583 - 0.0598 \cdot T)} \right) \tag{14}$$

$$\varepsilon_r(T) = \varepsilon_r(37°\mathrm{C}) \cdot \left(1 - \frac{1}{1 + \exp(5.223 - 0.0524 \cdot T)}\right) \quad (15)$$

Table 1 shows the dielectric and thermal properties employed for healthy tissue, tumor, and blood [8, 32, 43].

Table 1. Dielectric and thermal properties [8, 32, 43].

	ρ ($\mathrm{kg \cdot m^{-3}}$)	c ($\mathrm{J \cdot kg^{-1} \cdot K^{-1}}$)	k ($\mathrm{W \cdot m^{-2} \cdot K^{-1}}$)	σ_e(37°C) ($\mathrm{S \cdot m^{-1}}$)	ε_r(37°C) (-)
Healthy liver	1080 [a]	3455 [a]	0.502	1.95	57.55
	370 [b]	2156 [b]			
Tumor	1045 [a]	3760 [a]	0.600	2.18	62.44
	370 [b]	2156 [b]			
Blood	1000 [a]	3639 [a]			
	370 [b]	2156 [b]	0.502		

[a]At temperatures below 100°C and [b] above 100°C

About the boundary and initial conditions, null flux is set as a boundary condition in the symmetry axis for both thermal and electromagnetic problems. Both tissue and blood temperatures are considered to be 37 °C, at t = 0 s and for t > 0 at the remaining boundaries. The domain is set as large as to make edge effects negligible, thus the 37 °C uniform temperature boundary condition for t > 0 is reliable.

The effect of the antenna cooling circuit is modeled by applying a convective heat flux (q_c) to the cooling circuit boundary as follows:

$$q_c = h_r(T_r - T_t) \quad (16)$$

where h_r is the thermal convective coefficient (2838 W m^{-2} K^{-1}) which correspond to the low flow rate of 25 ml/min, T_t the tissue temperature and T_r the coolant temperature (20°C) as described in [44, 45].

A first-order scattering boundary condition is applied in the MWA electromagnetic problem at the outer boundaries and a null initial electric field value is employed. The MWA input power of 60 W is set as a coaxial port boundary condition at the top of the antenna. As regards the blood phase, uniform blood velocity is assumed in the four principal directions of the domain (i.e., *r*, *-r*, *z*, *-z*) in order to reproduce a more realistic in vivo isotropic vessel network. In addition, four different uniform vascularization types are included into the blood phase separately (capillaries, terminal arteries, terminal branches, and tertiary branches) corresponding to four different blood velocities and consequently blood vessel diameters, in order to appreciate the different outcomes obtained in the four different conditions. The vascular distribution varies as different parts of the organ are considered, so distinct uniform distributions are assessed. Table 2 shows the blood vessels diameters (*d*) and blood velocities (**u**) [46].

Table 2. Blood vessels diameters and the corresponding blood velocities used in the simulations (data from [46]).

	d (m)	**u** (m s^{-1})
Capillaries	$8 \cdot 10^{-6}$	$7 \cdot 10^{-4}$
Terminal arteries	$3 \cdot 10^{-5}$	$4 \cdot 10^{-3}$
Terminal branches	$5 \cdot 10^{-5}$	$2 \cdot 10^{-2}$
Tertiary branches	$1.4 \cdot 10^{-4}$	$3.4 \cdot 10^{-2}$

The coupled electromagnetic and thermal problems are numerically solved using the finite-element commercial software COMSOL Multiphysics (COMSOL, Burlington, MA, USA). The mesh consists of 14,388 triangular elements. The grid size is verified using a convergence test by increasing the number of elements from 3597 to 28776. Figure 3 shows the temperature evolution at a specific point of the tumor rim (r = 1.2 cm, z = 0.0 cm) for the four cases of meshing, confirming the choice of 14388 elements.

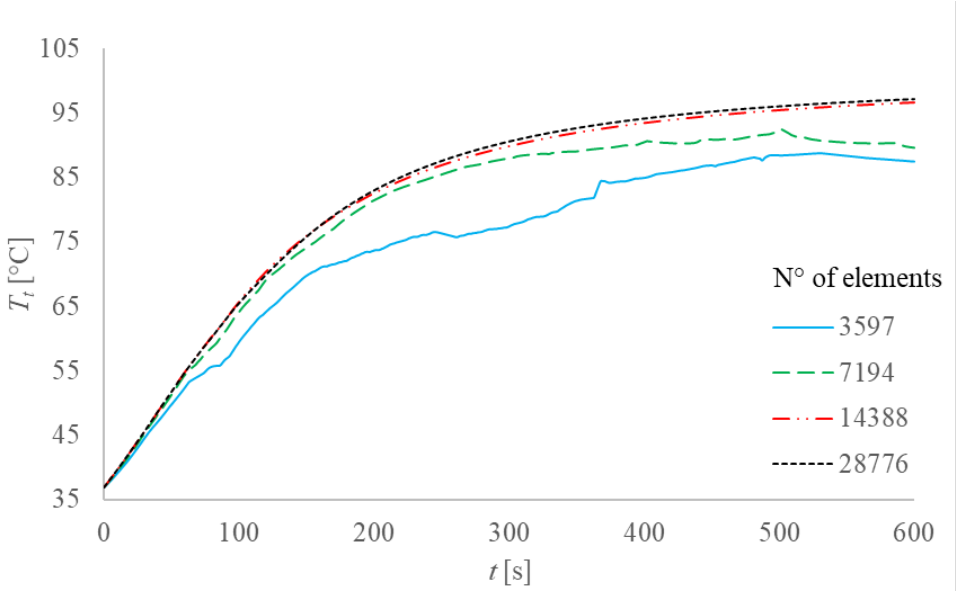

Figure 3. Grid convergence test on temperature profiles: temperature evolution evaluated at r = 1.2 cm and z = 0.0 cm for different number of elements considered (60 W, 10 min).

PARDISO direct solver is employed to solve governing equations, and second-order Lagrangian elements are used to discretize equations. About the time-stepping method, the intermediate backward differentiation formulas (BDF) is used, where the intermediate configuration was chosen to fix the initial and maximum steps of the solver, in this case 0.001 s and 0.4 s, respectively. As for the grid convergence, the effect of different time

steps is verified on four different minimum time steps, considering temperature profiles achieved in the tumor rim point (r = 0.012 m, z = 0 m) as shown in Figure 4 which confirms the choice made of 0.001 s.

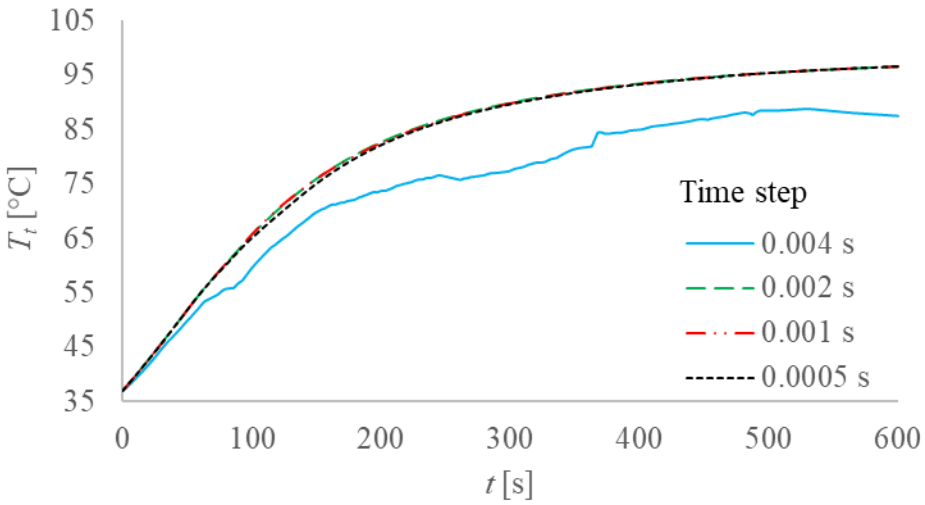

Figure 4. Time step convergence test on temperature profiles: temperature evaluated at r = 1.2 cm and z = 0.0 cm for different time steps (60 W, 10 min)

3. Results and discussion

In this section the results are shown in terms of temperature fields, transverse diameters of the ablation zone, and ablation volumes achieved considering the four different blood vessel types. Figures 5 shows the tissue temperature evolution every 150 s during MWA, considering capillaries, terminal arteries, terminal branches, and tertiary branches blood vessels that infiltrates through the tissue, respectively. The white line corresponds to the ablation contour, namely the Ω = 4.6 isoline, and it is clear that it becomes wider as tissue temperature increases for all the cases. Comparing the different vascularization types,

maximum temperatures and consequently larger ablation zones are obtained for capillaries (Figure 5, a-d), while the progressive temperature reduction can be observed for terminal arteries (Figure 5, e-h), terminal branches (Figure 5, i-l) and tertiary branches (Figure 5, m-p), which results in smaller ablation zones.

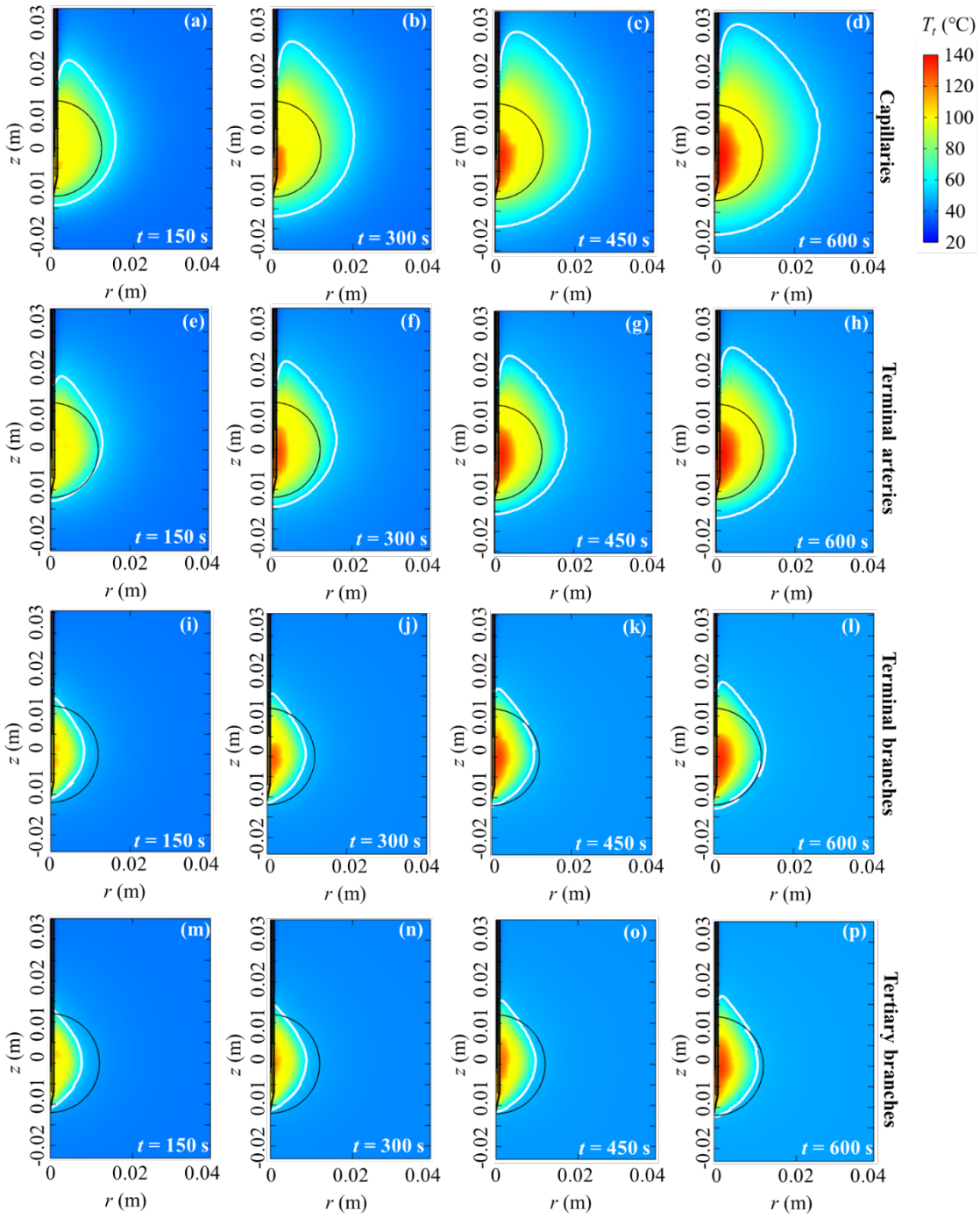

Figure 5. Temperature distribution evolution during MWA when capillaries (a-d), terminal arteries (e-h), terminal branches (i-l), and tertiary branches (m-p) are considered as blood vessels in the domain. The white line is the $\Omega = 4.6$ (99% cell death probability) contour, the black line is the tumor contour.

Moving from capillaries to tertiary branches, blood vessels diameters become larger and the blood velocity increases, so the heat removed from tissue phase by the blood phases increases too, resulting in a higher heat sink effect and smaller ablation zones achieved at the end of treatment, al already showed in [33]. Besides, in all the cases it is shown that the ablation zone is not perfectly spherical, but it is slightly elongated along the z direction due to the effect of power reflection at the open end of the antenna. Although the modeled antenna has a choke to reduce back heating effects, this is not totally removed.

As concerns the ablation zones, while for capillaries and terminal arteries the complete ablation is fully obtained, vascularization made up of terminal branches or tertiary branches makes this goal difficult to be achieved. In Table 3, transverse ablation diameters (in *r* direction of the domain) obtained at 300 s and 600 s are shown and compared with the experimental results from a clinical study [28] including 30 patients on who 32 tumors with mean diameter of 2.4 cm were ablated with MW using the same antenna and protocol as simulated here.

From Table 3 it can be clearly noticed that the results match the experimental results well by including terminal arteries in the model, confirming the reliability of the Chen and Holmes' LTNE model [47], in which blood heat exchange is assumed to occur only downstream of terminal arteries before the arterioles. Considering other types of vessels, the results differ from +43% to -43% as compared to the experimental ones, which

correspond to including capillaries and tertiary branches respectively. These results highlight the importance of an accurate modelling of the real vascularization of both tumor and healthy tissue, which plays a key role in the final outcomes.

Moreover, Table 3 shows that the results achieved for terminal arteries are more accurate than the outcomes obtained in [8] using Pennes' model in liver MWA with the same applicator, power, and duration. Thus, this model can achieve more accurate results than other bioheat models, and at the same time it can be adapted easier to different tissue morphologies including information on blood velocity, blood vessels' direction and dimensions which can be obtained in clinical practice before or even during the treatment.

Table 3. Ablation transverse diameters for different blood vessels in tissue domain.

		d_c [cm]		d_c deviation from [28] in %	
		60 W 300 s	60 W 600 s	60 W 300 s	60 W 600 s
Porous media model	Capillaries	4.1	5.3	+24%	+43%
	Terminal arteries	3.2	4.0	-3%	+8%
	Terminal branches	1.9	2.6	-42%	-30%
	Tertiary branches	1.8	2.1	-45%	-43%
Pennes' model	Trujillo et al. [8]	2.7	3.2	-18%	-13%
Clinical study	Amabile et al. [28]	3.3 ± 0.5	3.7 ± 0.3		

Concerning the ablation volumes obtained, they are directly calculated by making surface integrations of the 2D zones limited by the Ω = 4.6 (99% cell death probability) contours, across the azimuth angle as in [8]. Table 4 shows the ablation volumes computed for all the cases and their comparison with those reported in the clinical study [28]. From

Table 4, the vascular structure which matches the experimental results better is that one made up of terminal arteries again. The values obtained for this case, indeed, are included in the range of the experimental measures' uncertainties, both at the middle and at the end of treatment, even if the best performance of the numerical model is obtained after 600 s. This good agreement suggests that ablation zone is well-predicted in all the direction considered including the non-sphericity of the ablation zone. Furthermore, as for ablation zone transverse diameter, Table 4 displays that the ablation volumes obtained for terminal arteries are more accurate than the results achieved in [8] using Pennes' model in liver MWA with the same applicator design, power, and duration.

In Figure 6, the percentage of ablation volume on the total tumor volume is displayed for the entire duration of treatment, resulting in an almost linear evolution, with an increasing slope as the blood vessels become smaller. As regards the case which matches the experimental results better, namely for terminal arteries blood distribution, the linear fit equation is described by the equation:

$$\frac{V_{nec}}{V_{tum}} \times 100 = 0.752t + 19.5 \tag{17}$$

which gives an immediate knowledge of the ablated volume at a specific time of the treatment.

From Figure 6 it can be highlighted that the complete ablation of the tumor is achieved only when capillaries, terminal arteries and terminal branches are considered as blood phase which infiltrates into the tissue phase, after ~71 s, 107 s, and 529 s respectively, so the vascularization of the tissue to be ablated affects the duration and the success of the ablation treatment.

Table 4. Ablation volumes for different blood vessels in tissue domain.

		Ablation volume [cm^3]	
		60 W 300 s	60 W 600 s
Porous media model	Capillaries	35.9	72.2
	Terminal arteries	18.4	34.0
	Terminal branches	4.40	9.30
	Tertiary branches	3.20	5.80
Pennes' model	Trujillo et al. [8]	9.50	16.0
Clinical study	Amabile et al. [28]	27.4 ± 12.3	37.3 ±10.4

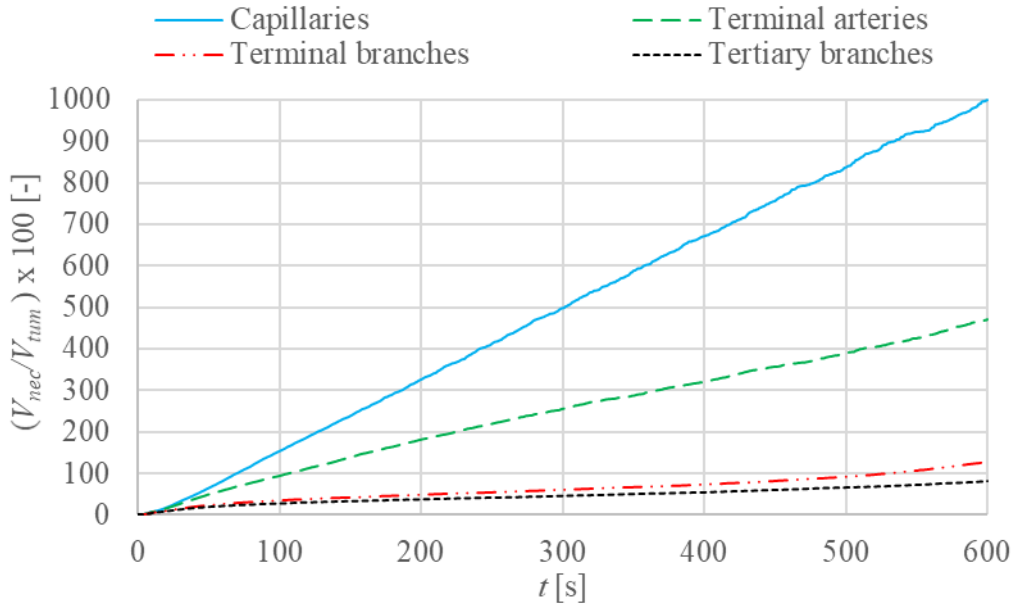

Figure 6. Evolution in time of necrotic volume percentage on total tumor volume.

As concerns the limitations of this study, first of all only one MW applicator is simulated, limiting the results and conclusions to this device. Nevertheless, it is widely used in clinical practice due to the large ablation zones obtained, so it effectively represents a reference

device for MWA. Different applicators can be considered in future works to confirm the performance of the model in distinct cases. Moreover, the exact vascularization of the target tissue is unknown, so different uniform distributions have been investigated. This shortcoming can be overcome including more precise information in the model thanks to imaging techniques applied before or during the treatment. Thanks to these future improvements the model will become more and more accurate for different types of tumors located in distinct vascularized zones, in order to be able to predict the ablation zone on a case by case basis, avoiding tumor recurrence and improving both medical protocols and devices.

4. Conclusions

In this work, a new porous media-based bioheat model is developed to simulate an *in vivo* MWA of a tumor liver tissue surrounded by healthy tissue. The blood volume fraction, namely the porosity, is here modeled for the first time in authors' knowledge as a quadratic function based on *in vivo* experimental measures which highlights the differences between the tumor core, the tumor rim, and the healthy tissue. Moreover, four different uniform vascularizations are considered in order to make the model more and more realistic and to appreciate the relevance of different blood vessels in tissue. The model is validated with an *in vivo* clinical study on 30 human patients with hepatocellular carcinoma, carried out with the same protocol and probe. The results in terms of ablation diameters, ablation volumes and temperature profiles show that the terminal arteries vascularization achieves very accurate results in terms of ablation diameter (-3% and +8% after 300 s and 600 s respectively). This model can represent a reference point for *in vivo* thermal ablation modelling because it overcomes the limitations of different bioheat models in literature,

achieving accurate results and at the same time allowing to be adapted easily to different tissues' morphologies which includes distinct vascularizations.

Declaration of interest: The authors declare that they have no known competing financial interests or personal relationships that could have influenced the work reported in this paper.

Funding details: This work was supported by the Grant RTI2018-094357-B-C21 funded by MCIN/AEI/ 10.13039/501100011033and by the Italian Government MIUR Grant N° "PRIN-2017F7KZWS".

This work was also supported by the *Università degli Studi di Napoli Federico II* international mobility program for researchers.

References

[1] Chu, K. F., & Dupuy, D. E. (2014). Thermal ablation of tumours: biological mechanisms and advances in therapy. Nature Reviews Cancer, 14(3), 199-208.

[2] Brace, C. (2011). Thermal tumor ablation in clinical use. IEEE pulse, 2(5), 28-38.

[3] Diederich, C. J. (2005). Thermal ablation and high-temperature thermal therapy: overview of technology and clinical implementation. International journal of hyperthermia, 21(8), 745-753.

[4] Nikfarjam, M., Muralidharan, V., & Christophi, C. (2005). Mechanisms of focal heat destruction of liver tumors. Journal of Surgical Research, 127(2), 208-223.

[5] Andreozzi, A., Iasiello, M., & Tucci, C. (2020). An overview of mathematical models and modulated-heating protocols for thermal ablation.

[6] Markezana, A., Ahmed, M., Kumar, G., Zorde-Khvalevsky, E., Rozenblum, N., Galun, E., & Goldberg, S. N. (2020). Moderate hyperthermic heating encountered during thermal ablation increases tumor cell activity. International Journal of Hyperthermia, 37(1), 119-129.

[7] Markezana, A., Ahmed, M., Kumar, G., Zorde-Khvalevsky, E., Rozenblum, N., Galun, E., & Goldberg, S. N. (2020). Moderate hyperthermic heating encountered during thermal ablation increases tumor cell activity. International Journal of Hyperthermia, 37(1), 119-129.

[8] Trujillo, M., Prakash, P., Faridi, P., Radosevic, A., Curto, S., Burdio, F., & Berjano, E. (2020). How large is the periablational zone after radiofrequency and microwave ablation? Computer-based comparative study of two currently used clinical devices. International Journal of Hyperthermia, 37(1), 1131-1138.

[9] Pennes, H. H. (1948). Analysis of tissue and arterial blood temperatures in the resting human forearm. Journal of applied physiology, 1(2), 93-122.

[10] Andreozzi, A., Brunese, L., Iasiello, M., Tucci, C., & Vanoli, G. P. (2019). Modeling heat transfer in tumors: a review of thermal therapies. Annals of biomedical engineering, 47(3), 676-693.

[11] Berjano, E. J. (2006). Theoretical modeling for radiofrequency ablation: state-of-the-art and challenges for the future. Biomedical engineering online, 5(1), 1-17.

[12] Andreozzi, A., Brunese, L., Iasiello, M., Tucci, C., & Vanoli, G. P. (2019, May). Bioheat transfer in a spherical biological tissue: a comparison among various

models. In Journal of Physics: Conference Series (Vol. 1224, No. 1, p. 012001). IOP Publishing.

[13] Tucci, C., Trujillo, M., Berjano, E., Iasiello, M., Andreozzi, A., & Vanoli, G. P. (2021). Pennes' bioheat equation vs. porous media approach in computer modeling of radiofrequency tumor ablation. Scientific Reports, 11(1), 1-13.

[14] Vafai, K. (Ed.). (2015). Handbook of porous media. Crc Press.

[15] Xuan, Y., & Roetzel, W. (1997). Bioheat equation of the human thermal system. Chemical Engineering & Technology: Industrial Chemistry-Plant Equipment-Process Engineering- Biotechnology, 20(4), 268 -276.

[16] Khaled, A. R., & Vafai, K. (2003). The role of porous media in modeling flow and heat transfer in biological tissues. International Journal of Heat and Mass Transfer, 46(26), 4989-5003.

[17] Khanafer, K., & Vafai, K. (2006). The role of porous media in biomedical engineering as related to magnetic resonance imaging and drug delivery. Heat and mass transfer, 42(10), 939-953.

[18] Nakayama, A., & Kuwahara, F. (2008). A general bioheat transfer model based on the theory of porous media. International Journal of Heat and Mass Transfer, 51(11-12), 3190-3199.

[19] Keangin, P., & Rattanadecho, P. (2013). Analysis of heat transport on local thermal non-equilibrium in porous liver during microwave ablation. International Journal of Heat and Mass Transfer, 67, 46-60.

[20] Rattanadecho, P., & Keangin, P. (2013). Numerical study of heat transfer and blood flow in two-layered porous liver tissue during microwave ablation process using

single and double slot antenna. International Journal of Heat and Mass Transfer, 58(1-2), 457-470.

[21] Dombrovsky, L. A., Timchenko, V., Jackson, M., & Yeoh, G. H. (2011). A combined transient thermal model for laser hyperthermia of tumors with embedded gold nanoshells. International Journal of Heat and Mass Transfer, 54(25-26), 5459-5469.

[22] Andreozzi, A., Brunese, L., Iasiello, M., Tucci, C., & Vanoli, G. P. (2020). A novel local thermal non-equilibrium model for biological tissue applied to multiple-antennas configurations for thermal ablation. Numerical Heat Transfer, Part A: Applications, 79(2), 111-121.

[23] Wang, K., Tavakkoli, F., Wang, S., & Vafai, K. (2015). Analysis and analytical characterization of bioheat transfer during radiofrequency ablation. Journal of biomechanics, 48(6), 930-940.

[24] Mahjoob, S., & Vafai, K. (2009). Analytical characterization of heat transport through biological media incorporating hyperthermia treatment. International Journal of Heat and Mass Transfer, 52(5-6), 1608-1618.

[25] Chung, S., & Vafai, K. (2014). Mechanobiology of low-density lipoprotein transport within an arterial wall—impact of hyperthermia and coupling effects. Journal of biomechanics, 47(1), 137-147.

[26] AlAmiri, A., Khanafer, K., & Vafai, K. (2014). Fluid-structure interactions in a tissue during hyperthermia. Numerical Heat Transfer, Part A: Applications, 66(1), 1-16.

[27] Stewart, E. E., Chen, X., Hadway, J., & Lee, T. Y. (2006). Correlation between hepatic tumor blood flow and glucose utilization in a rabbit liver tumor model. Radiology, 239(3), 740-750.

[28] Amabile, C., Ahmed, M., Solbiati, L., Meloni, M. F., Solbiati, M., Cassarino, S., Tosoratti, N., Nissenbaum, Y., Ierace, T., & Goldberg, S. N. (2017). Microwave ablation of primary and secondary liver tumours: ex vivo, in vivo, and clinical characterisation. International Journal of Hyperthermia, 33(1), 34-42.

[29] Amiri, A., & Vafai, K. (1994). Analysis of dispersion effects and non-thermal equilibrium, non-Darcian, variable porosity incompressible flow through porous media. International journal of heat and mass transfer, 37(6), 939-954.

[30] Yuan, P. (2008). Numerical analysis of temperature and thermal dose response of biological tissues to thermal non-equilibrium during hyperthermia therapy. Medical engineering & physics, 30(2), 135-143.

[31] Chang, I. A. (2010). Considerations for thermal injury analysis for RF ablation devices. The open biomedical engineering journal, 4, 3.

[32] Zhang, B., Moser, M. A., Zhang, E. M., Luo, Y., & Zhang, W. (2015). Numerical analysis of the relationship between the area of target tissue necrosis and the size of target tissue in liver tumours with pulsed radiofrequency ablation. International Journal of Hyperthermia, 31(7), 715-725.

[33] Andreozzi, A., Brunese, L., Iasiello, M., Tucci, C., & Vanoli, G. P. (2021). Numerical analysis of the pulsating heat source effects in a tumor tissue. Computer Methods and Programs in Biomedicine, 200, 105887.

[34] Andreozzi, A., Brunese, L., Iasiello, M., Tucci, C., & Vanoli, G. P. (2021). Numerical Investigation of a Thermal Ablation Porous Media-Based Model for Tumoral Tissue with Variable Porosity. Computation, 9(5), 50.

[35] Cuenod, C. A., & Balvay, D. (2013). Perfusion and vascular permeability: basic concepts and measurement in DCE-CT and DCE-MRI. Diagnostic and interventional imaging, 94(12), 1187-1204.

[36] Taniguchi, H., Masuyama, M., Koyama, H., Oguro, A., & Takahashi, T. (1996). Quantitative measurement of human tissue hepatic blood volume by C15O inhalation with positron-emission tomography. Liver, 16(4), 258 -262.

[37] Dobson, E. L., Warner, G. F., Finney, C. R., & Johnston, M. E. (1953). The measurement of liver circulation by means of the colloid disappearance rate: I. Liver blood flow in normal young men. Circulation, 7(5), 690-695.

[38] Schwickert, H. C., Roberts, T. P., Shames, D. M., Dijke, C. F. V., Disston, A., Mühler, A., ... & Brasch, R. C. (1995). Quantification of liver blood volume: comparison of ultra short TI inversion recovery echo planar imaging (ULSTIR- EPI), with dynamic 3D-gradient recalled echo imaging. Magnetic resonance in medicine, 34(6), 845-852.

[39] Abraham, J. P., & Sparrow, E. M. (2007). A thermal-ablation bioheat model including liquid-to-vapor phase change, pressure-and necrosis-dependent perfusion, and moisture-dependent properties. International Journal of Heat and Mass Transfer, 50(13-14), 2537-2544.

[40] Smith, S. R., Foster, K. R., & Wolf, G. L. (1986). Dielectric properties of VX-2 carcinoma versus normal liver tissue. IEEE transactions on biomedical engineering, (5), 522-524.

[41] Woodard, H. Q., & White, D. R. (1986). The composition of body tissues. The British journal of radiology, 59(708), 1209-1218.

[42] Lopresto, V., Pinto, R., Farina, L., & Cavagnaro, M. (2017). Microwave thermal ablation: effects of tissue properties variations on predictive models for treatment planning. Medical engineering & physics, 46, 63-70.

[43] O'rourke, A. P., Lazebnik, M., Bertram, J. M., Converse, M. C., Hagness, S. C., Webster, J. G., & Mahvi, D. M. (2007). Dielectric properties of human normal, malignant and cirrhotic liver tissue: in vivo and ex vivo measurements from 0.5 to 20 GHz using a precision open-ended coaxial probe. Physics in medicine & biology, 52(15), 4707.

[44] González-Suárez, A., Trujillo, M., Burdío, F., Andaluz, A., & Berjano, E. (2012). Feasibility study of an internally cooled bipolar applicator for RF coagulation of hepatic tissue: Experimental and computational study. International Journal of Hyperthermia, 28(7), 663-673.

[45] Radosevic, A., Prieto, D., Burdío, F., Berjano, E., Prakash, P., & Trujillo, M. (2021). Short pulsed microwave ablation: computer modeling and ex vivo experiments. International Journal of Hyperthermia, 38(1), 409-420.

[46] Crezee, J., & Lagendijk, J. J. W. (1992). Temperature uniformity during hyperthermia: the impact of large vessels. Physics in Medicine & Biology, 37(6), 1321.

[47] Chen, M. M., & Holmes, K. R. (1980). Microvascular contributions in tissue heat transfer. Annals of the New York Academy of Sciences, 335(1), 137-150.